Preprint 2/26/20, published as: B.Wang, K. Aryana, J. T. Gaskins, P. E. Hopkins, S. V. Khare, and D. Gall, Adv. Funct. Mater. **30**, 2001915 (2020). https://doi.org/10.1002/adfm.202001915

Structural stabilization and piezoelectric enhancement in epitaxial $(Ti_{1-x}Mg_x)_{0.25}Al_{0.75}N(0001)$ layers

Baiwei Wang,[a] Kiumars Aryana,[b] John T. Gaskins,[b] Patrick E. Hopkins,[b] Sanjay V. Khare,[c] Daniel Gall[a]

[a] *Department of Materials Science and Engineering, Rensselaer Polytechnic Institute, Troy, NY 12180, USA*
[b] *Department of Mechanical and Aerospace Engineering, University of Virginia, Charlottesville, Virginia 22904, USA*
[c] *Department of Physics and Astronomy, University of Toledo, 2801 West Bancroft Street, Toledo, OH, 43606, USA*

Epitaxial $(Ti_{1-x}Mg_x)_{0.25}Al_{0.75}N(0001)/Al_2O_3(0001)$ layers are used as a model system to explore how Fermi-level engineering facilitates structural stabilization of a host matrix despite the intentional introduction of local bonding instabilities that enhance the piezoelectric response. The destabilizing octahedral bonding preference of Ti dopants and the preferred 0.67 nitrogen-to-Mg ratio for Mg dopants deteriorate the wurtzite AlN matrix for both Ti-rich ($x < 0.2$) and Mg-rich ($x \geq 0.9$) alloys. Conversely, $x = 0.5$ leads to a stability peak with a minimum in the lattice constant ratio c/a which is caused by a Fermi-level shift into the bandgap and a trend towards non-directional ionic bonding, leading to a maximum in the expected piezoelectric stress constant e_{33}. The refractive index and the sub-gap absorption decrease with x, the optical band gap increases, and the elastic constant along the hexagonal axis $C_{33} = 270 \pm 14$ GPa remains composition independent, leading to an expected piezoelectric constant $d_{33} = 6.4$ pC/N at $x = 0.5$ which is 50% larger than for the pure AlN matrix. Thus, contrary to the typical anti-correlation between stability and electromechanical coupling, the $(Ti_{1-x}Mg_x)_{0.25}Al_{0.75}N$ system exhibits simultaneous maxima in the structural stability and the piezoelectric response at $x = 0.5$.

TOC entry:

$(Ti_{1-x}Mg_x)_{0.25}Al_{0.75}N(0001)$ layers exhibit a maximum in the piezoelectric constant d_{33} at $x = 0.5$ which is 50% larger than that of pure AlN and is attributed to Ti and Mg dopants destabilizing the local bonding symmetry. Simultaneously, $x = 0.5$ yields a stability peak with a minimum vertical lattice constant c as the Fermi level moves into the band gap.

TOC figure:

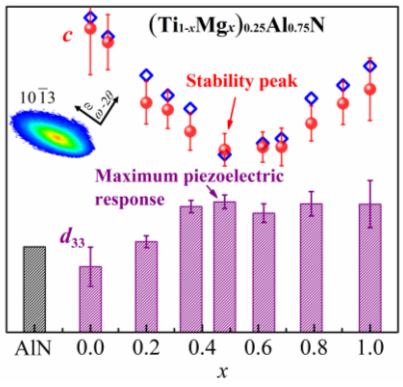

1. Introduction

AlN exhibits a large spontaneous polarization at zero strain and a piezoelectric/pyroelectric response under stress/temperature variations which is due to the broken inversion symmetry along the *c* axis of its wurtzite structure in combination with the strong ionicity of the aluminum-nitrogen bond.[1] In addition, AlN has a low dielectric loss and a high acoustic velocity and breakdown voltage, making it suitable for AlN-based devices including thin film bulk acoustic resonators, surface acoustic wave guides and vibrational energy harvesters.[2] The substitutional incorporation of additional elements in AlN can considerably enhance its response to external stimuli.[1a] For example, the incorporation of Sc to form a ternary $Al_{1-x}Sc_xN$ yields a four-fold increase in the piezoelectric response in comparison to pure AlN.[3] This is attributed to a softening[4] and destabilization[5] of the hexagonal AlN wurtzite structure by addition of Sc atoms which tend towards nearly five-fold-coordinated atomic positions like in h-ScN.[6] This causes a reduction in the elastic constant C_{33} and a simultaneous increase in the internal strain sensitivity and therefore the piezoelectric stress constant e_{33}, yielding an overall enhancement of the piezoelectric coefficient $d_{33} \approx e_{33}/C_{33}$. However, the high cost and low abundance of Sc impedes the wide application of $Al_{1-x}Sc_xN$ and motivates exploration of alternative alloying elements. First-principles calculations suggest that the simultaneous introduction of bivalent (e.g. Mg, Ca and Zn) and tetravalent (e.g. Ti, Zr, Hf and Si) elements can serve as a replacement to trivalent Sc by providing a similar structure instability and enhanced piezoelectric response.[5] This has been confirmed experimentally by a measured increase in d_{33} when alloying AlN to form quaternaries including (Ti, Zn)AlN,[7] (Hf, Mg)AlN,[8] (Nb, Mg)AlN,[4c, 9] (Zr, Mg)AlN,[10] and (Ti, Mg)AlN[7, 11] while, in contrast, single dopants like Ti or Mg in AlN deteriorate the crystalline quality and are ineffective in increasing d_{33}.[7, 11] In addition, ferroelectric switching with a remnant polarization in excess of 100 $\mu C/cm^2$ was recently reported for $Al_{1-x}Sc_xN$,[12] indicating the potential for ferroelectric wurtzite-type AlN-based solid solutions and their integration into piezoelectric multilayer

actuator stacks,[13] non-volatile memory cells,[14] polar nitride heterojunction transistors,[15] multiferroic composites[16] and optoelectronic quantum structures.[17] However, despite the unique combination of semiconducting, piezoelectric, pyroelectric and ferroelectric properties and the good compatibility with current integrated circuit technology, relatively little is known about the synthesis, structure and optoelectronic properties of wurtzite-type AlN based quaternary alloys, which motivates the present study.

In this paper, we report on the growth and properties of epitaxial $(Ti_{1-x}Mg_x)_{0.25}Al_{0.75}N(0001)$ layers ($0.0 \leq x \leq 1.0$) on $Al_2O_3(0001)$ substrates by reactive magnetron co-sputtering from titanium, magnesium and aluminum targets in 5 mTorr pure N_2 at 700 °C. We chose an aluminum rich composition with 75% of the metal atoms being Al, in order to facilitate crystallization in the wurtzite structure which is polar and is therefore expected to exhibit the desired piezoelectric properties. X-ray diffraction ω-2θ scans, ω-rocking curves, φ-scans, and reciprocal space maps show that wurtzite $(Ti_{1-x}Mg_x)_{0.25}Al_{0.75}N$ layers with $0.0 \leq x \leq 0.8$ are epitaxial single crystals, while extra peaks from a secondary phase emerge for layers with $x = 0.9$ and 1.0. The crystalline quality of wurtzite $(Ti_{1-x}Mg_x)_{0.25}Al_{0.75}N$ increases with increasing x due to a high Mg surface diffusivity and the same fourfold local coordination preference for Mg as for Al. The lattice parameter c along growth direction [0001] decreases with increasing $x < 0.5$ but increases for $x > 0.5$, yielding a distinct "v" shape that demonstrates the stabilization of the wurtzite structure at $x = 0.5$. Optical analyses indicate an increasing bandgap and a decreasing refractive index with increasing x. These results suggest that the stabilization at $x = 0.5$ is associated with the Fermi-level being near or in the gap, which results in occupied bonding and empty antibonding orbitals. The measured C_{33} is nearly composition independent while the measured lattice constant ratio indicates a maximum in e_{33} at $x = 0.5$, resulting in an expected peak in d_{33} at $x = 0.5$ that is 50% larger than d_{33} of the AlN matrix.

2. Results

Figure 1 shows the results from the compositional analysis done by photoelectron spectroscopy. The measured Mg-content x in the $(Ti_{1-x}Mg_x)_{0.25}Al_{0.75}N$ layers is plotted vs the ratio P_{Mg}/P_{Ti} of power applied to the Mg and Ti targets during deposition. x increases steeply as P_{Mg} is increased from 0 to 20 W while keeping $P_{Mg} + P_{Ti} = 50$ W constant, and then more moderately as P_{TiN} is decreased to 20, 10 and 0 W with a constant $P_{Mg} = 20$ W, as also summarized in the table inside Figure. 1. The plotted data points are well described by the expression $x = 1/[1 + \alpha \times (P_{Mg}/P_{Ti})^{-1}]$, which is shown as dashed line and corresponds to the expected composition under the assumption that the Mg and Ti atomic fluxes to the substrate are proportional to the power applied to the deposition sources. The data fitting provides a value for $\alpha = 0.26$, which corresponds to the ratio of the Ti vs Mg sputter deposition rate at $P_{Mg} = P_{Ti}$. This indicates that the sputter rate of Ti in a N_2 plasma is approximately four times smaller than for Mg, consistent with the reported ratio of 0.3, estimated based on the cohesive energy of the elementary metals.[18] The table in Figure. 1 also lists the measured Al content, which is defined as the fraction of Al with respect to all cations (Ti+Mg+Al) in the compounds. It is 0.75 ± 0.03 for all layers. Correspondingly, we use the notation $(Ti_{1-x}Mg_x)_{0.25}Al_{0.75}N$ to represent all samples presented in this paper. The measured N-to-metal ratio decreases from 0.96 ± 0.02 for $x = 0$ to 0.86 ± 0.02 for $x = 0.48$ and 0.82 ± 0.02 for $x = 1.00$, which is attributed to the tendency for Mg nitride to be metal-rich, as discussed in section IV.

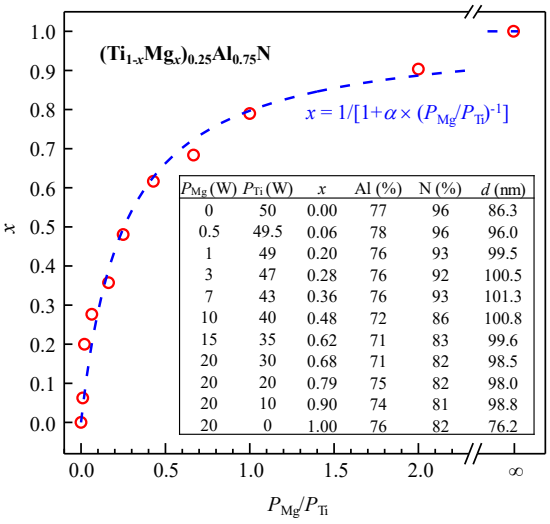

P_{Mg} (W)	P_{Ti} (W)	x	Al (%)	N (%)	d (nm)
0	50	0.00	77	96	86.3
0.5	49.5	0.06	78	96	96.0
1	49	0.20	76	93	99.5
3	47	0.28	76	92	100.5
7	43	0.36	76	93	101.3
10	40	0.48	72	86	100.8
15	35	0.62	71	83	99.6
20	30	0.68	71	82	98.5
20	20	0.79	75	82	98.0
20	10	0.90	74	81	98.8
20	0	1.00	76	82	76.2

Figure 1. The Mg content x in $(Ti_{1-x}Mg_x)_{0.25}Al_{0.75}N$ layers vs the ratio P_{Mg}/P_{Ti} of power applied to the Mg and Ti targets during deposition. The table in the inset lists the measured composition and thickness d for each sample. The Al and N content are given relative to the total metal content, i.e. the sum of Mg+Ti+Al is set to 100%.

Figure 2(a) shows sections of typical x-ray diffraction ω-2θ patterns for 2θ = 33-37° and 40-42° from $(Ti_{1-x}Mg_x)_{0.25}Al_{0.75}N$ layers with x = 0.00 - 1.00, as labeled. The intensity is plotted on a logarithmic scale and the scans are offset vertically for clarity purposes. The double peak feature at 41.686° and 41.802° is from the substrate sapphire 0006 reflections of the Cu $K\alpha_1$ and $K\alpha_2$ lines, while the less intense peaks at smaller angles are the 0002 reflections from the $(Ti_{1-x}Mg_x)_{0.25}Al_{0.75}N$ layers. For all samples with $x \leq 0.79$, the only detected layer peaks within the entire measured 2θ range of 5 - 85° are the plotted 0002 reflections, indicating a strong preferred 0001 orientation and, together with data shown in Figure. 2(b) and (c), confirming that the $(Ti_{1-x}Mg_x)_{0.25}Al_{0.75}N$ layers in our study are epitaxial. The pattern from the $Ti_{0.25}Al_{0.75}N$ layer (x = 0.00) has a peak at 34.94°, corresponding to a lattice constant c = 5.131 Å. Replacing some of the Ti with Mg to form $(Ti_{1-x}Mg_x)_{0.25}Al_{0.75}N$ alloys yields similar XRD patterns but with a continuous peak shift to higher 2θ-values of 35.05°, 35.27°, 35.39°, 35.46°, and 35.73° for x = 0.06, 0.20, 0.28, 0.36, and 0.48, indicating a decreasing c = 5.116, 5.085, 5.069, 5.059, and 5.022 Å. Increasing the Mg content beyond a Mg-to-Ti ratio of 1:1 results in a reversal of the peak shift to 2θ = 35.66°, 35.64°, 35.40°, 35.33° and 35.22° for x = 0.62, 0.68, 0.79, 0.90, and 1.00, indicating an increasing c = 5.031, 5.035, 5.067, 5.077, and 5.093 Å. In addition, an increasing Mg content results in narrower and more intense 0002 peaks, with a measured peak full-width at half-maximum (FWHM) $\Gamma_{2\theta}$ = 0.81° for pure $Ti_{0.25}Al_{0.75}N$ and $\Gamma_{2\theta}$ = 0.48°, 0.48°, 0.35°, and 0.33° for x = 0.20, 0.48, 0.79 and 1.00, and a corresponding intensity that is 7, 12, 8 and 6 times stronger than for x = 0.00.

Figure 2(b) shows a typical XRD ω rocking curve of the 0002 reflection from the $(Ti_{0.10}Mg_{0.90})_{0.25}Al_{0.75}N$ layer, which is obtained using a constant 2θ = 35.32°. Its FWHM Γ_ω = 0.74° is within the range 0.02 – 2.6° of reported values for epitaxial AlN(0001)/Al_2O_3(0001) layers[19] and indicates a strong crystalline alignment of the $(Ti_{0.10}Mg_{0.90})_{0.25}Al_{0.75}N$ 0001 planes. Figure 2(d) is a plot of the measured 0002 ω rocking curve width for all samples in this study,

plotted as a function of composition x. It is relatively large, 4.8°, for the $Ti_{0.25}Al_{0.75}N$ layer and decreases to Γ_ω = 3.0°, 2.4°, 2.4°, 1.8°, 1.9°, 1.9°, 1.5°, 1.7°, 0.74°, and 0.93° with increasing x = 0.06, 0.20, 0.28, 0.36, 0.48, 0.62, 0.68, 0.79, 0.90 and 1.00, respectively.

Figure 2(c) shows a typical XRD φ-scan of the asymmetric $10\bar{1}1$ reflections from a $(Ti_{0.10}Mg_{0.90})_{0.25}Al_{0.75}N$ layer. It is acquired by recording the reflected intensity as a function of the azimuthal angle φ, using a 62.05° offset in χ and fixed 2θ = 37.74° and ω = 18.87° values. The pattern exhibits six peaks at φ = -150°, -90°, -30°, 30°, 90°, and 150°, indicating a 6-fold rotational symmetry. Figure. 2(c) also includes a φ-scan from the same sample, however, with 2θ, ω and χ adjusted to detect the substrate Al_2O_3 $10\bar{1}2$ reflections. This scan shows three peaks that are 10^3 times more intense and occur at φ values that are shifted by 30° relative to the $(Ti_{0.10}Mg_{0.90})_{0.25}Al_{0.75}N$ $10\bar{1}1$ reflections. This demonstrates, in combination with the results from Figure. 2(a) and (b), that the $(Ti_{0.10}Mg_{0.90})_{0.25}Al_{0.75}N$ layer exhibits an epitaxial layer-substrate relationship with $(0001)_{TiMgAlN}||(0001)_{Al2O3}$ and $[10\bar{1}0]_{TiMgAlN}||[1\bar{1}20]_{Al2O3}$. The same epitaxial relationship has previously been reported for AlN(0001) growth on Al_2O_3(0001)

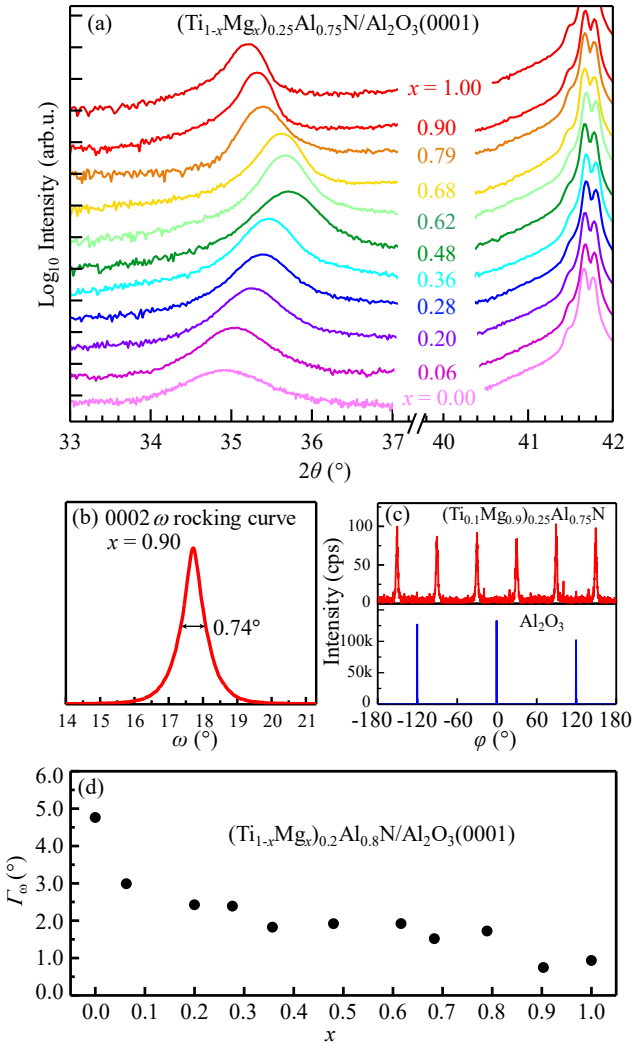

Figure 2. X-ray diffraction (a) ω-2θ scans, (b) typical ω rocking curve of the 0002 reflection, (c) typical φ-scan of $10\bar{1}1$ reflections, and (d) peak width Γ_ω of the 0002 ω rocking curves vs composition x from epitaxial $(Ti_{1-x}Mg_x)_{0.25}Al_{0.75}N(0001)$ layers on $Al_2O_3(0001)$.

where the 30° rotation reduces the in-plane lattice mismatch from -35% to +13%.[1b, 20] Similar XRD φ-scans were also obtained for other samples, confirming that all layers in this study are epitaxial.

Figure 3 is shows the measured lattice constants a and c of $(Ti_{1-x}Mg_x)_{0.25}Al_{0.75}N(0001)$ layers as a function of composition x, plotted as magenta and red circles, respectively. They are determined from x-ray diffraction reciprocal space maps (RSMs) around asymmetric $10\bar{1}3$ reflections. The plot also includes the c values determined from the 0002 peaks in the ω-2θ scans shown in Figure. 2(a). They are plotted as blue open diamonds labeled $c_{\omega\text{-}2\theta}$ and are in good agreement (0.01-0.53% deviation) with the red dots from the RSMs. A typical RSM around the $10\bar{1}3$ reflection from a $(Ti_{0.64}Mg_{0.36})_{0.25}Al_{0.75}N$ layer is shown as inset at the top of Figure. 3. It is a logarithmic-scale color filled iso-intensity contour map in k-space where $k_\perp = 2\sin\theta\cos(\omega\text{-}\theta)/\lambda$ and $k_\parallel = 2\sin\theta\sin(\omega\text{-}\theta)/\lambda$ correspond to directions perpendicular and parallel to the substrate surface corresponding to [0001] and $[10\bar{1}0]$ directions in the layer, as indicated by the labeled arrows. The plot also includes a scale bar in units of reciprocal length and arrows indicating the experimental ω-2θ and ω scan directions.[21] The elliptical shape of the $(Ti_{0.74}Mg_{0.36})_{0.25}Al_{0.75}N$ $10\bar{1}3$ reflection can be described by peak broadening along the two primary ω-2θ and ω scan directions, which are rotated by 32.11° from the $k_\perp$ and $k_\parallel$ directions. The broadening along ω-2θ is attributed to local strain variations and the finite layer thickness, while broadening along

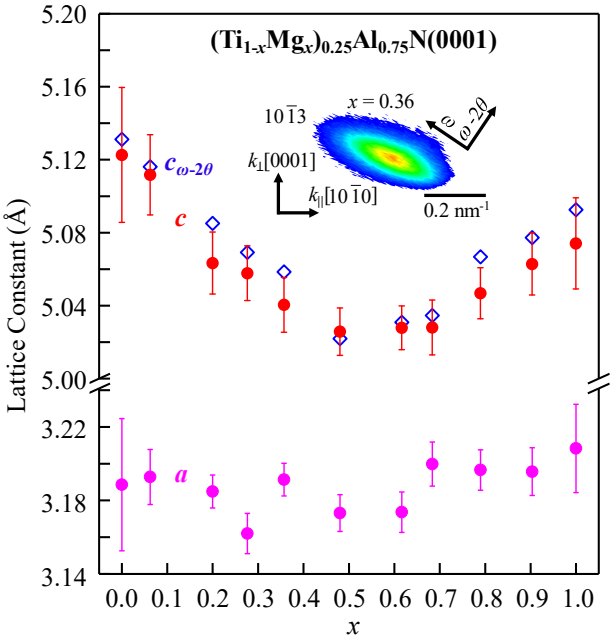

Figure 3. Out-of-plane c and in-plane a lattice constants obtained from RSMs (red and magenta circles) and c obtained from ω-2θ scans (blue open diamonds) vs Mg content x in $(Ti_{1-x}Mg_x)_{0.25}Al_{0.75}N(0001)/Al_2O_3(0001)$.

ω is primarily due to the mosaic spread, that is, the misalignment of crystallites which are single crystal blocks within the epitaxial $(Ti_{0.74}Mg_{0.36})_{0.25}Al_{0.75}N$ layer.[22] The out-of-plane and in-plane lattice constants c and a are determined from the measured peak position $k_{\perp} = 5.952$ nm^{-1} and $k_{||} = 3.618$ nm^{-1} using $c = 3/k_{\perp} = 5.040 \pm 0.015$ Å and $a = (2/\sqrt{3})/k_{||} = 3.191 \pm 0.010$ Å for the $(Ti_{0.74}Mg_{0.36})_{0.25}Al_{0.75}N$ layer. The former value agrees within experimental uncertainty with $c_{\omega\text{-}2\theta} = 5.059 \pm 0.002$ Å determined from the ω-2θ scan from the same sample. We note that the uncertainties in a and c from the RSM are larger than for $c_{\omega\text{-}2\theta}$, due to the difficulty in accurately determining the center of the $10\bar{1}3$ reflections in the reciprocal space map.

The measured c decreases with increasing $x < 0.5$ but increases for $x > 0.5$, yielding a distinct "v" shape when considering the whole composition range $0.0 \leq x \leq 1.0$. In contrast, a remains approximately constant within the experimental uncertainty, ranging from 3.16 - 3.21 Å. The $Ti_{0.25}Al_{0.75}N$ layer ($x = 0.00$) has a $c = 5.131 \pm 0.002$ Å and 5.123 ± 0.040 Å as determined from the ω-2θ scan and RSM, respectively, and an $a = 3.189 \pm 0.040$ Å. These values agree with the previously reported lattice constants $c = 5.12$-5.15 Å and $a = 3.15$-3.18 Å for wurtzite $Ti_{0.25}Al_{0.75}N$ layers.[23] We measure a c to a ratio $c/a = 1.606$ for $Ti_{0.25}Al_{0.75}N$, which is very close to the known $c/a = 4.9792$ Å / 3.1114 Å $= 1.600$ for AlN.

Figure 4(a) is a photograph of the $(Ti_{1-x}Mg_x)_{0.25}Al_{0.75}N/Al_2O_3(0001)$ samples, sorted according to their composition x. It shows the visual appearance of the deposited layers, indicating a progressively increasing transparency with increasing x, with the color transitioning form brown yellow for $x = 0.00$ to light yellow for $x = 0.48$ and transparent for $x = 1.00$, consistent with the measured optical absorption presented below. Figure. 4(b) and (c) show typical UV-Vis transmittance T and reflectance R spectra from three representative $(Ti_{1-x}Mg_x)_{0.25}Al_{0.75}N$ layers with $x = 0.00$, 0.48 and 1.00 in the photon range $\hbar\omega = 2.0$ - 6.5 eV. The $Ti_{0.25}Al_{0.75}N$ ($x = 0.00$) layer shows a high-transmission plateau with $T = 0.44 \pm 0.01$ for $2.0 < \hbar\omega < 2.45$ eV, followed a continuous decrease to $T = 0.05$ at $\hbar\omega = 4.65$ eV. The spectra

from the other samples are qualitatively similar but show a higher maximum transmission and a shift to higher photon energies for both the maximum T and the drop in T. More specifically, the maximum $T = 0.72 \pm 0.01$ at $\hbar\omega = 2.55$ eV for $x = 0.48$ and $T = 0.74 \pm 0.03$ at $\hbar\omega = 3.85$ eV for $x = 1.00$, and the transmission is reduced to 0.05 at $\hbar\omega = 4.90$ and 6.4 eV, respectively. Several minor oscillations such as those at $\hbar\omega \approx 4.5$, 4.0, and 5.5 eV in the T spectra for layers with $x = 0.00$, 0.48, and 1.00, are opposite to the oscillations in the measured R and are therefore attributed to interference fringes from multiple internal reflections. The reflectance spectra in Figure. 4(c) are dominated by Fresnel fringes due to the interference from reflection at the air/layer and layer/substrate interfaces. The amplitude of the fringes decreases and the fringes gradually disappear with increasing $\hbar\omega$, consistent with the decreasing T in Figure. 4(b) and the increasing absorption coefficient discussed below. The minor discontinuities at $\hbar\omega = 2.58$, 3.30, and 3.88 eV in the R spectra are experimental artifacts due to the switch of the optical gratings and the associated beam shift.

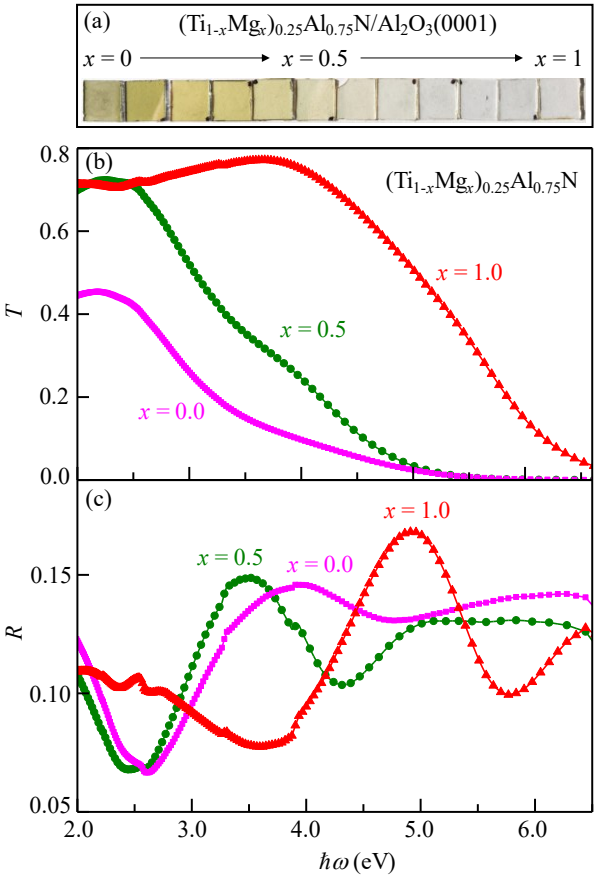

Figure 4. Optical (a) photograph (b) transmittance T and (c) reflectance R vs photon energy $\hbar\omega$ for $(Ti_{1-x}Mg_x)_{0.25}Al_{0.75}N$ layers.

Figure 5 is a plot of the refractive index n of $(Ti_{1-x}Mg_x)_{0.25}Al_{0.75}N(0001)$ layers as a function of Mg content x. It is determined from the interference fringes in the measured reflectance spectra for a wavelength $\lambda = 400$ nm. All samples are quite transparent at $\lambda = 400$ nm, such that n can be directly determined from the spacing between interference fringe minima

and maxima and the measured layer thickness. This method yields $n = 2.08$ for a pure AlN control sample (not shown), which is in good agreement with the reported range for the refractive index of AlN at λ = 400 nm of n = 1.98 – 2.15.[24] The plotted refractive index decreases with increasing Mg content from $n = 2.79$ for the $Ti_{0.25}Al_{0.75}N$ ($x = 0$) layer to $n = 2.68$, 2.59, 2.42, and 2.20 for the $(Ti_{1-x}Mg_x)_{0.25}Al_{0.75}N$ alloys with $x = 0.28$, 0.48, 0.79, and 1.00, respectively. The decrease is approximately linear for $0.0 \le x \le 0.79$, as illustrated in the plot with a fit through the data points corresponding to $n = 2.78 - 0.45x$. The measured n deviates from the linear trend for $x = 0.90$ and 1.00, which we attribute to the emergence of a secondary phase at high Mg content, as detected by XRD.

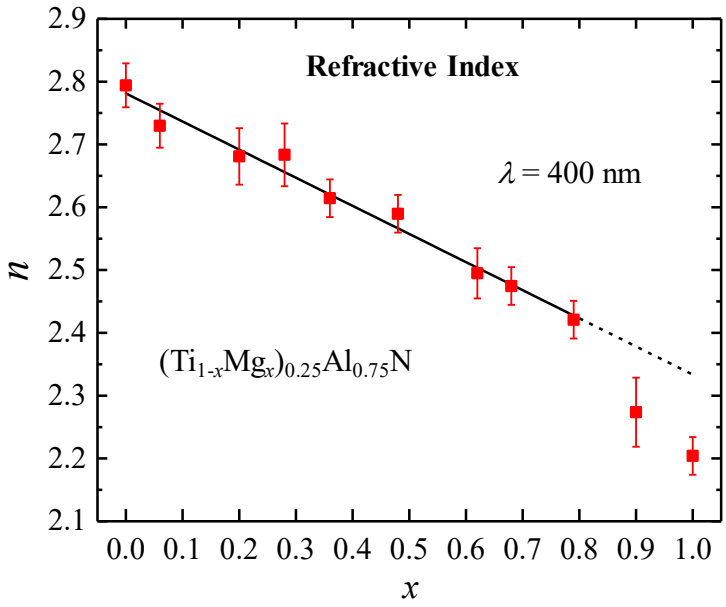

Figure 5. Refractive index n at a wavelength of 400 nm vs composition x of $(Ti_{1-x}Mg_x)_{0.25}Al_{0.75}N$ layers.

Figure 6(a) is a plot of the optical absorption coefficient α vs photon energy $\hbar\omega$ = 2.0-6.5 eV, as determined from T and R spectra of $(Ti_{1-x}Mg_x)_{0.25}Al_{0.75}N$ layers. The absorption for the $Mg_{0.25}Al_{0.75}N$ ($x = 1$) layer exhibits a steep increase in α at $\hbar\omega > 5.3$ eV, which is attributed to interband transitions. This interpretation is based on a similar measured onset in α from a pure AlN layer (not shown) at larger $\hbar\omega > 6.1$ eV, which is within the range of previously reported AlN band gap values of 5.90 - 6.25 eV[1b, 25] and suggests that the substitution of Al by Mg to form $Mg_{0.25}Al_{0.75}N$ reduces the band gap. The plotted absorption for the $x = 0.9$ alloy exhibits an absorption onset around $\hbar\omega = 4.8$ eV, indicating that replacing Mg with Ti further reduces the bandgap. This trend is continued with decreasing x, leading to a monotonically

decreasing absorption edge which reaches 3.5 eV for $Ti_{0.25}Al_{0.75}N$ ($x = 0$). The plotted curves for $x < 0.5$ indicate an additional absorption between $\hbar\omega = 3$ and 4 eV which we attribute to mid-gap states and/or disorder induced band tails that cause sub-bandgap absorption for Ti rich alloys, as discussed below. The position of the absorption edge is quantitatively evaluated using the Tauc's plot method,[26] as illustrated in the inset of Figure. 6(b) for a $(Ti_{0.52}Mg_{0.48})_{0.25}Al_{0.75}N$ layer.

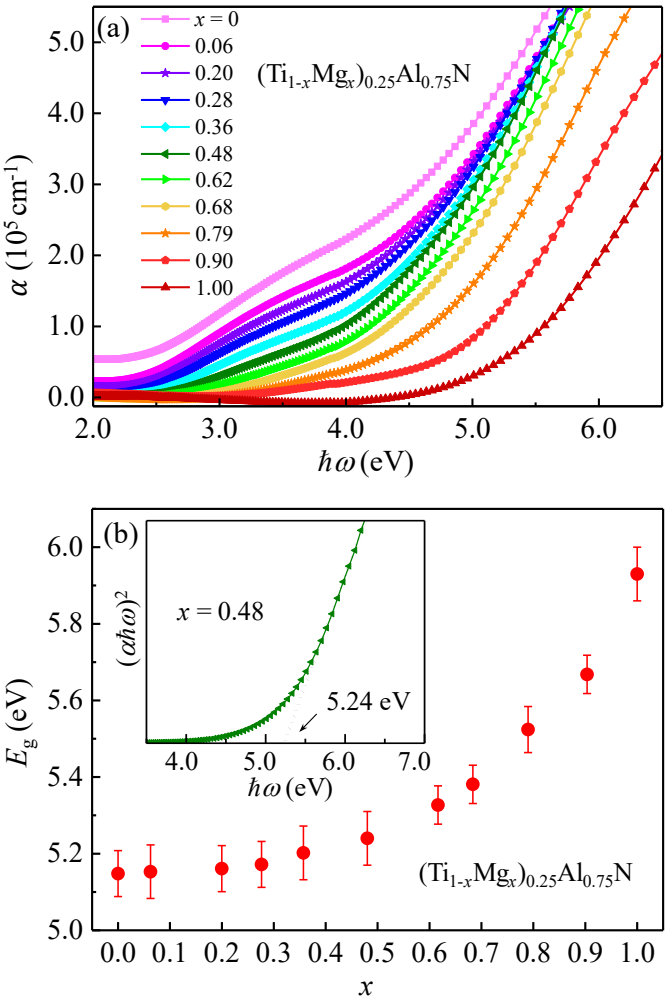

Figure 6. (a) Optical absorption coefficient α vs photon energy $\hbar\omega$ and (b) optical band gap E_g vs x from $(Ti_{1-x}Mg_x)_{0.25}Al_{0.75}N$ layers with $0.00 \le x \le 1.00$. The inset shows a Tauc plot used to determine E_g.

The linear extrapolation of the $(\alpha\hbar\omega)^2$ vs $\hbar\omega$ curve yields a value for the optical gap $E_g = 5.24$ eV for $x = 0.48$. The main plot of Figure. 5(b) shows the optical band gap of $(Ti_{1-x}Mg_x)_{0.25}Al_{0.75}N$ layers as a function of x. It increases slightly with increasing $x < 0.5$, and then more steeply with $x > 0.5$, from $E_g = 5.15$ eV for $x = 0$ to $E_g = 5.93$ eV for $x = 1$.

Figure 7 shows the elastic constant C_{33}, piezoelectric stress constant e_{33}, and the piezoelectric coefficient d_{33}, as a function of x in $(Ti_{1-x}Mg_x)_{0.25}Al_{0.75}N$ layers. The top right inset is a typical time resolved thermoreflectivity plot for the $Ti_{0.12}Mg_{0.13}Al_{0.75}N(0001)$ layer. It shows the measured change in thermoreflectance R_T as a function of delay time Δt of the probe

beam, where $\Delta t = 0$ is the time at which the pump and the probe hit the surface at the same time, causing an increase in temperature at the sample surface due to the sub-picosecond thermal excitation in the aluminum. Two well-developed peaks at Δt = 22.4 and 44.5 ps are attributed to the signature of reflected waves from the Al/film and film/substrate interfaces, respectively. The time of 22.1 ps between these two reflections corresponds to the time required for a

longitudinal wave to travel from the aluminum/film interface to the film/substrate interface and then back to the aluminum/film interface. A sound velocity v_{0001} = 9.1 km/s is calculated from this time delay and the thickness d = 100.8 nm for this x = 0.48 layer. The measured velocity is

for the longitudinal wave travelling perpendicular to the layer surface, which corresponds to the [0001] crystallographic direction along the hexagonal axis of $(Ti_{1-x}Mg_x)_{0.25}Al_{0.75}N(0001)$. The measured v_{0001} is approximately 10% smaller than the reported v_{0001} = 10.2-11.1 km/s for AlN,[2a] and is comparable to v_{0001} = 9.5 km/s reported for a $(Zr, Mg)_{0.13}Al_{0.87}N$ layer.[10c] We determine the mass density ρ = 3.29 g/cm^3 from the measured composition and lattice constants a and c for this x = 0.48 layer, to obtain the matrix

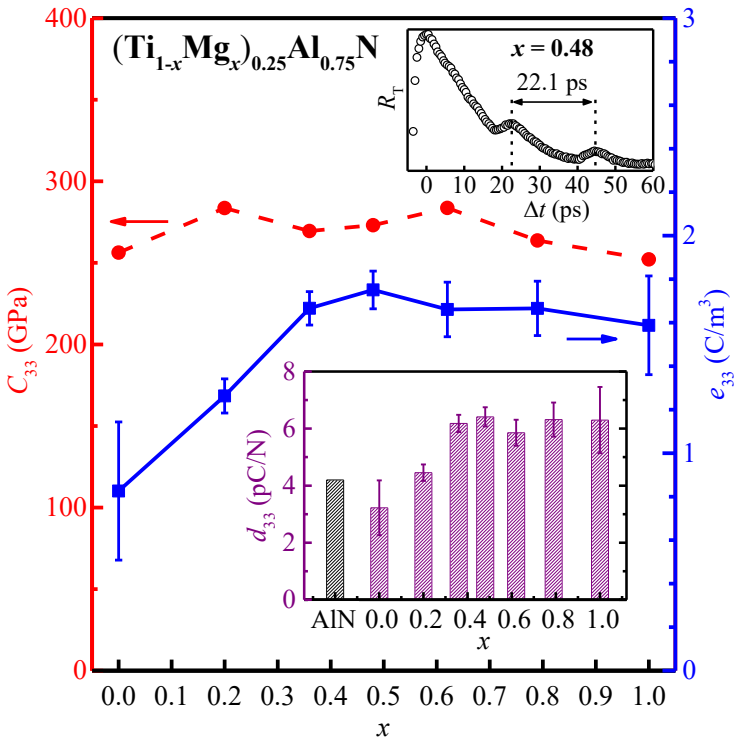

Figure 7. The elastic constant C_{33} (red circles) and piezoelectric stress constant e_{33} (blue squares) of $(Ti_{1-x}Mg_x)_{0.25}Al_{0.75}N$ layers with $0.00 \le x \le 1.00$. The top inset shows the measured thermoreflectance signal R_T vs pump-probe time delay Δt from the layer with x = 0.48, and the bottom inset is a bar-plot of the piezoelectric coefficient d_{33} vs x in $(Ti_{1-x}Mg_x)_{0.25}Al_{0.75}N$. The black bar indicates d_{33} for pure AlN from Ref. [17].

element $C_{33} = \rho v_{0001}^2 = 273 \pm 2$ GPa of the elastic tensor that relates normal stress and resultant strain along [0001]. Correspondingly, C_{33} is determined for all $(Ti_{1-x}Mg_x)_{0.25}Al_{0.75}N(0001)$ layers in this study and plotted as red circles in Figure. 7. It is nearly independent of x, varying between 252 and 284 GPa, with an average $C_{33} = 270 \pm 14$ GPa for all compositions $x = 0.0$-1.0. Figure. 7 also includes e_{33} (blue squares) estimated from the measured c-to-a ratio using the reported relationship $e_{33} = Z_v \times [(c/a)_o - c/a]$ where $(c/a)_o = \sqrt{8/3} = 1.633$ is the lattice constant ratio for an ideal wurtzite structure and $Z_v = 34.75$ C/m^2 is a coefficient related to the nominal ionic valences[4c, 9, 27] and is obtained from $e_{33} = 1.75$ C/m^2 for $(Ti_{0.5}Mg_{0.5})_{0.25}Al_{0.75}N$ ($x = 0.5$) that was previously determined by first-principles calculations.[5a] The plotted e_{33} increases from 0.8 C/m^2 for $Ti_{0.25}Al_{0.75}N$ ($x = 0$) to $e_{33} = 1.3$ and 1.7 C/m^2 for $x = 0.20$ and 0.36, reaches a maximum of 1.8 C/m^2 for $x = 0.48$ followed by a decrease to $e_{33} = 1.7$, 1.7, and 1.6 C/m^2 for $x = 0.62$, 0.79, and 1.00, respectively. The piezoelectric coefficient is estimated using $d_{33} \approx e_{33}/C_{33}$, and is plotted in the inset in Figure. 7. It exhibits a similar composition dependence as e_{33}, since C_{33} is nearly independent of x. More specifically, d_{33} increases from 3.2 to 4.5 and 6.2 pC/N for $x = 0$, 0.20 and 0.36, reaches a maximum of $d_{33} = 6.4$ pC/N for $x = 0.48$, and decreases to 5.9, 6.3, 6.3 pC/N for $x = 0.62$, 0.79, and 1.00, respectively. The inset also includes as black bar the reported $d = 4.2$ pC/N for AlN,[5a, 27-28] illustrating that the maximum piezoelectric response for $(Ti_{1-x}Mg_x)_{0.25}Al_{0.75}N$ layers at $x = 0.5$ is 50% larger than that of the pure AlN matrix.

3. Discussion

The crystalline quality of $(Ti_{1-x}Mg_x)_{0.25}Al_{0.75}N(0001)$ alloy layers increases with increasing Mg content, as indicated by narrower and more intense 0002 ω-2θ peaks and ω rocking curves in Figure. 2(a) and (d). We attribute this to (i) a higher surface diffusivity for Mg than Ti, based on their melting points of 650 and 1670 °C, respectively, and (ii) the

difference in the local coordination geometry preference between Mg and Ti.[5a] More specifically, Ti tends to have a six-fold local coordination number with N,[29] while Mg and Al typically bond with four nitrogen nearest neighbors.[5a, 30] As a consequence, Ti atoms in AlN tend to destabilize the four-fold local atomic arrangement which leads to the reported phase separation for $Al_{1-y}Ti_yN$ alloys with $y > 28 \pm 5\%$.[31] The phase separation is driven by a thermodynamic instability of the (Ti,Al)N wurtzite solid solution and is facilitated by surface diffusion,[31d] similar to what has been reported for other immiscible systems like wurtzite (Al, Zr)N.[32] The $Ti_{0.25}Al_{0.75}N$ layer ($x = 0$) is our sample with the highest Ti content and is close to the phase separation limit, which explains its wide rocking curve width. Increasing x corresponds to the substitution of Ti with Mg atoms which mitigates the local instability because of the fourfold coordination preference of Mg, leading to the measured decrease in Γ_ω with increasing x. However, at high $x = 0.90$ and 1.00, the XRD analyses reveal an additional broad and weak peak at $2\theta = 37.5$ - 40.0°, suggesting an emerging secondary phase similar to what has been reported for ternary $Al_{1-x}Mg_xN$ ($x \geq 0.14$) and $Al_{1-x}Nb_xN$ ($x \geq 0.20$) and quaternary $Mg_xNb_yAl_{1-x-y}N$ ($x \geq 0.35$, $y \geq 0.22$) layers.[7, 9, 11] Thus, the solubility of Mg in wurtzite AlN is also limited. We attribute this to the N-to-metal ratio of the most stable pure magnesium nitride phase (Mg_3N_2) to be 0.67, which is lower than the 1.00 for stoichiometric AlN and TiN. This affects the N-to-metal ratio in the $(Ti_{1-x}Mg_x)_{0.25}Al_{0.75}N$ alloys which we measure to decrease from approximately stoichiometric for $x = 0$ to 0.82 ± 0.02 for $x = 1.0$, as summarized in the table in Figure. 1. The decreasing N-to-metal ratio corresponds to an increasing N vacancy concentration with increasing x, which affects the Fermi level and, in turn, the onset of optical absorption as discussed below. A similar increase in nitrogen vacancies during Mg incorporation into AlN and GaN has been reported previously.[11, 33]

The plotted lattice constant c vs composition x in $(Ti_{1-x}Mg_x)_{0.25}Al_{0.75}N$ in Figure. 3 exhibits a characteristic "v" shape with a minimum at $x = 0.5$. The decreasing c for $x < 0.5$ is

opposite to the expectation based on the lager atomic radius for Mg (1.51-1.77 Å) than for Ti (1.44-1.49 Å),[34] but is consistent with the reported right-shift of 0002 reflections from $Mg_xNb_{1-x}Al_{0.27}N$ with x = 0.39-0.44.[9] We attribute the decrease to elastic softening along the crystal c direction[4c, 5a] and the competition between bonding and anti-bonding states as the Fermi level E_f decreases with increasing x in $(Ti_{1-x}Mg_x)_{0.25}Al_{0.75}N$.[35] More specifically, simple electron counting suggests that a 50-50 Ti-to-Mg ratio leads to a vanishing carrier density, with E_f for $(Ti_{0.5}Mg_{0.5})_{0.25}Al_{0.75}N$ in the bandgap, while $x < 0.5$ and $x > 0.5$ result in highly degenerated n and p-type semiconductors, respectively.[5b, 21] The Fermi level for $Ti_{0.25}Al_{0.75}N$ (x = 0) is in the conduction band,[31a] yielding 0.25 electrons per formula unit occupying anti-bonding states. As x is increased, each substitution of a Ti by a Mg atom reduces the number of electrons in the conduction band by two, resulting in a decrease in E_f and a corresponding reduction in the occupied anti-bonding states. This results in a reduction in c to reach a minimum at x = 0.5 when E_f is in the band gap and all anti-bonding states are depleted. A further increase in $x > 0.5$ yields a continuing decrease of E_f in the valence band, and therefore a reduction in the number of electrons in bonding states. This lowers the bond strength, leading to the measured lattice constant increase for Mg-rich samples from c = 5.026 Å for x = 0.48 to c = 5.074 Å for pure $Mg_{0.25}Al_{0.75}N$ (x = 1.00). The latter value is in excellent agreement with 5.075±0.003 Å determined from linear interpolation of the reported c-values from $Mg_{0.16}Al_{0.84}N$ and $Mg_{0.30}Al_{0.70}N$ alloys.[36] We note that the increase in N vacancies with increasing x reduces the shift of E_f to lower energies, partially compensating the effect of replacing Ti with Mg atoms such that E_f for $x > 0.5$ is closer to the band gap than would be expected when only considering the Mg and Ti content.

The structural shrinking and expansion with changing composition is anisotropic, since the decrease and increase in c are not replicated in a, which remains constant within experimental uncertainty for the entire $0 \leq x \leq 1$ range. This is attributed to a destabilization of the AlN wurtzite structure by substitutional Mg and Ti atoms, associated with a transition from

directional sp^3-hybridized to isotropic ionic bonding.[1b] The destabilization in the $(Ti_{1-x}Mg_x)_{0.25}Al_{0.75}N$ system is noteworthy because it exhibits a composition range for which the Ti and/or Mg concentration is large enough to cause nonlinear structural changes while small enough to suppress phase separation. Correspondingly, the resulting layers are single-phase ($x < 0.90$) but structurally destabilized, representing a promising composition for a large piezoelectric response, as discussed more in detail below.

The refractive index of $(Ti_{1-x}Mg_x)_{0.25}Al_{0.75}N$ alloys decreases approximately linearly with increasing x with $n = 2.78\text{-}0.45x$ for $x \leq 0.79$, as shown in Figure. 5. This decrease is attributed to (i) the decrease in the layer density with increasing Mg content which results in a lower electron density and correspondingly smaller electronic polarization, similar to the reported trends for $Al_{1-x}Sc_xN$[37] and $Al_{1-x}Y_xN$,[38] and (ii) the increasing bandgap, which results in a reduced intermixing of valence and conduction band states and therefore causing weaker electronic polarization.

The band gap in $(Ti_{1-x}Mg_x)_{0.25}Al_{0.75}N$ alloys increases with x, as determined by optical absorption and plotted in Figure. 6(b). The measured optical gap corresponds to the sum of (i) the gap between the valence band maximum (VBM) and the conduction band minimum (VBM) and (ii) the Moss-Burstein shift which is affected by the position of the Fermi level E_f. More specifically, starting from pure AlN, E_f is at the VBM[39] and the 6.05 eV gap between VBM and CBM defines the optical bandgap. Adding Mg to form a $Mg_{0.25}Al_{0.75}N$ alloy reduces the number of valence electrons and shifts E_f to lower energies, that is into the VB. However, our $Mg_{0.25}Al_{0.75}N$ layer contains a considerable fraction of N vacancies, as detected by the XPS compositional analysis. The N vacancies are expected to act as n-type dopants[40] which correspondingly cause charge compensation and an increase in E_f towards the VBM. If charge compensation is complete, E_f reaches the VBM and the measured E_g = 5.93 eV for the $Mg_{0.25}Al_{0.75}N$ layer corresponds to the VBM-to-CBM fundamental gap. Otherwise, the fundamental gap is smaller than the measured 5.93 eV. In both cases, the gap of $Mg_{0.25}Al_{0.75}N$

is below that of pure AlN, indicating that Mg reduces the gap between the VBM and CBM. This is expected, based on the considerably smaller gap of the pure Mg nitride, which has been reported to be 2.2 – 2.8 eV for cubic Mg_3N_2.[41] Replacing Mg with Ti atoms increases the number of electrons in the valence band such that $(Ti_{1-x}Mg_x)_{0.25}Al_{0.75}N$ becomes a semiconductor at $x = 0.5$. Correspondingly, E_f moves up and reaches the VBM at $x = 0.5$, causing the measured gap to decrease from 5.93 to 5.24 eV as x decreases from 1.0 to 0.5. The further addition of Ti atoms pushes E_f into the conduction band (for $x < 0.5$) such that the measured E_g corresponds to the transition between the VBM and E_f. Figure. 6 indicates a negligible slope of E_g vs x for $x < 0.5$, suggesting that the narrowing between VBM and CBM is compensated by the increase of E_f with decreasing x. Our results yield $E_g = 5.15$ eV for $Ti_{0.25}Al_{0.75}N$. This is slightly larger than the reported 4.87 eV from a polycrystalline $Ti_{0.25}Al_{0.75}N$ sample[25b] and may be attributed to band tails associated with grain boundaries or other defects in the sample of the previous report. We estimate a Moss-Burnstein shift of ~0.7 eV for $Ti_{0.25}Al_{0.75}N$ by assuming that the band structure of the alloy remains comparable to that of AlN[42] and that each Ti atom provides one electron to the conduction band. This yields an estimated gap between VBM and CBM of 4.5 eV for $Ti_{0.25}Al_{0.75}N$. We note that Ti rich samples are the most conductive, with a measured resistivity of 169 and 256 Ω·cm for $(Ti_{1-x}Mg_x)_{0.25}Al_{0.75}N$ samples with $x = 0.00$ and 0.06, respectively, while all the other samples with higher Mg content ($x > 0.06$) are too insulating to be measured with our 4-point probe setup. In addition, Ti rich samples exhibit sub-bandgap absorption, as evidenced in the α spectra for $x < 0.5$ at $\hbar\omega \approx 3$ - 4 eV shown in Figure. 6(a), suggesting mid-gap states that are introduced by Ti atoms. This is consistent with reported first-principles calculation studies which indicate that 3*d* orbitals of Ti create states in the band gap of $Ti_{0.03}Mg_{0.03}Al_{0.94}N$ such that the gap between the valence band maximum and these states is 33% smaller than the gap of pure AlN.[5b] Thus, it becomes an open question if the high conductivity of $Ti_{0.25}Al_{0.75}N$ is due to a

conductive mid-gap impurity band caused by the Ti atoms or if they serve as *n*-dopants that turn the layer into a heavily degenerate semiconductor with transport in the conduction band.

The elastic constant C_{33} along the [0001] growth direction is nearly independent of x, which leads to maxima in e_{33} and d_{33} due to the minimum in the measured c/a ratio at $x = 0.5$. Our measured values of $c/a = 1.583$, $\rho = 3.29$ g/cm^3 and $C_{33} = 273$ GPa for the $x = 0.48$ sample is in good agreement with previously reported first-principles predictions of $c/a = 1.58$, $\rho = 3.31$g/cm^3[5b] and $C_{33} = 255$ GPa.[5a] Our estimated $d_{33} = 6.4$ pC/N for $x = 0.48$ is 1.5 times larger than the reported $d_{33} = 4.2$ pC/N for AlN,[5a, 27-28] in good agreement with the reported theoretical prediction of a 1.6-fold enhancement in d_{33}.[5a] Our d_{33} is slightly (7%) higher than the previously reported $d_{33} = 6$ pC/N from a textured MgTi-doped-AlN layer with (Mg+Ti) = 25 % and Mg/Ti = 1.[11] This difference can be attributed to experimental uncertainty but may also indicate that the higher crystalline quality and phase purity of the epitaxial layers in our study yield an enhanced d_{33}, consistent with previous reports which propose crystalline quality improvements as a key strategy to improve the d_{33} in AlN-based ternary and quaternary alloys.[5a, 8c, 9] The C_{33} for $(Ti_{1-x}Mg_x)_{0.25}Al_{0.75}N$ alloys is 1.5 times smaller than for AlN, which we attribute to elastic softening of the wurtzite structure by substitutional Ti and Mg atoms. A similar dopant-induced softening along the c axis of AlN has been reported for several related materials systems including $Al_{1-x}Sc_xN$,[4b, 5a] (Ti, Zn)AlN,[7] (Hf, Mg)AlN,[8] (Nb, Mg)AlN,[4c, 9] and (Zr, Mg)AlN.[10] The quasi-binary alloy layers at the end points of our compositional sample series, $Ti_{0.25}Al_{0.75}N$ ($x = 0$) and $Mg_{0.25}Al_{0.75}N$ ($x = 1$), have d_{33} values that are 23% below and 50% above d_{33} for AlN, in good agreement with previous experimental reports for polycrystalline 0001-textured layers.[11, 36, 43] The low d_{33} for $x = 0$ is primarily attributed to Ti as a single dopant to not be effective in decreasing the c/a ratio, leading to a low e_{33} for $Ti_{0.25}Al_{0.75}N$. In contrast, $(Ti_{1-x}Mg_x)_{0.25}Al_{0.75}N$ alloys particularly with $x = 0.5$ (and to a certain extent $x > 0.5$) have larger e_{33} values, which can be attributed to a maximum competition between different local coordination geometries. More specifically, previously reported first-

principle studies indicate a strong linear correlation between e_{33} and the difference between calculated energies for the cubic zinc-blende minus the layered hexagonal structure for various AlN-based quaternary nitrides.[5a] These two structures are possible transformation products for the wurtzite structure under tensile or compressive stress, with fourfold or fivefold local coordination geometry. We expect this competition to reach a maximum at $x = 0.5$ while, in parallel, $x = 0.5$ also stabilizes the wurtzite structure since a 50/50 mixture of tetravalent Ti and bivalent Mg serves as a perfect replacement to trivalent Al. Thus $x = 0.5$ provides a unique composition point for a maximized piezoelectric response in a stabilized wurtzite structure.

4. Conclusions

The alloy with $x = 0.5$ in wurtzite structure $(Ti_{1-x}Mg_x)_{0.25}Al_{0.75}N$ represents a uniquely stable composition. This is shown using epitaxial $(Ti_{1-x}Mg_x)_{0.25}Al_{0.75}N(0001)$ layers with $0.0 \leq x \leq 1.0$ that are grown on $Al_2O_3(0001)$ substrates by reactive magnetron co-sputtering from titanium, magnesium and aluminum targets in 5 mTorr pure N_2 at 700 °C. X-ray diffraction reciprocal space maps show that the in-plane lattice constant is composition independent while the out-of-plane lattice constant c exhibits a minimum at $x = 0.5$, yielding a characteristic "v" shape in the c vs x plot. This suggests a high stability of the $(Ti_{0.5}Mg_{0.5})_{0.25}Al_{0.75}N$ alloy. In contrast, Ti-rich compositions result in a low crystalline quality, as quantified by the XRD rocking curve width. This is attributed to the preference of Ti atoms to form 6 (rather than 4) bonds with nitrogen, causing a destabilization of the local bond structure of the AlN matrix. Similarly, Mg-rich $(Ti_{1-x}Mg_x)_{0.25}Al_{0.75}N$ alloys are also not suited for high-quality crystals because of the nucleation of secondary phases, which are attributed to the lower nitrogen content of the stable Mg vs Al nitride (Mg_3N_2 vs AlN).

The measured refractive index at a wavelength $\lambda = 400$ nm decreases linearly according to $n = 2.78\text{-}0.45x$ for $x \leq 0.79$, which is attributed to the decreasing density. The optical band gap increases slightly from $E_g = 5.15$ to 5.24 eV for $x = 0.0$ to 0.5, but then much more steeply

to E_g = 5.93 eV for x = 1.0. The nearly constant E_g for $x < 0.5$ is attributed to an increase in the fundamental gap between valence band maximum and conduction band minimum that is compensated by a decrease in the Moss-Burnstein shift associated with a decreasing Fermi-level in the conduction band, consistent with a measured decreasing sub-gap absorption with increasing $x < 0.5$. The subsequent increase in E_g for $x > 0.5$ is attributed to an increase in the fundamental gap while the Fermi-level remains at or near the valence band maximum, as the expected decreasing electron density with increasing x is compensated by N vacancies, as detected by XPS compositional analyses. The overall results suggest that the maximum stability for x = 0.5 is associated with the Fermi-level being near or in the gap, which results in filled bonding and empty antibonding orbitals. The elastic constant shows an overall 1.5-fold decrease as compared to AlN and the piezoelectric stress constant e_{33} as well as piezoelectric constant d_{33} exhibit a maximum at x = 0.5, leading to a 50% higher piezoelectric response than for pure AlN. Thus, x = 0.5 in $(Ti_{1-x}Mg_x)_{0.25}Al_{0.75}N$ alloys represents a unique composition where both the structural stability and the piezoelectric stress response show simultaneous maxima, representing a promising material for piezoelectric applications.

5. Experimental Procedure

$(Ti_{1-x}Mg_x)_{0.25}Al_{0.75}N$ layers were deposited by reactive magnetron co-sputtering in a load-locked ultra-high vacuum deposition system with a base pressure of 10^{-9} Torr.[44] Double-side polished 10×10×0.5 mm^3 single-crystal *c*-plane sapphire $Al_2O_3(0001)$ substrates were cleaned in sequential ultrasonic baths of tri-chloroethylene, acetone, and isopropyl alcohol, for 20 min each, rinsed in de-ionized water, blown dry with nitrogen, mounted onto a Mo substrate holder using silver paint, and inserted into the deposition system. Prior to deposition, substrates were degassed for 1 hour at 1000 °C using a radiative pyrolytic graphite heater. Subsequently, the heater current was adjusted to reach the desired substrate temperature of 700 °C, as measured by a thermocouple underneath the substrate holder. 99.999% pure N_2, which was further

purified with a MicroTorr purifier, was introduced into the chamber with a needle valve to reach a constant pressure of 5 mTorr, as measured with a capacitance manometer. 5-cm-diamter nominally 99.99% pure Ti, Al, and Mg targets were positioned 9, 23, and 9 cm from the substrate surface with -45°, 0°, and +45° tilt angles, respectively. All three targets were sputter etched for 5 min prior to deposition, using 100 W on each magnetron with a shutter shielding the substrate. An AlN deposition rate of 2.8 nm/min was achieved using a constant power of 800 W from an Advanced Energy MDX 1.5K dc power supply with a Sparc-LE 20 pulse module operating in Self-Run mode to neutralize target charging by reversing the potential to the target with a 20 kHz frequency, a 90% duty cycle, and a reversed 10% voltage level. The dc power applied to the Ti and Mg targets were adjusted to achieve the desired composition range. Layers with low Mg concentrations were deposited using a partially (1/10, 1/5 and 1/2) opened shutter in front of the Mg target to achieve an equivalent power of 0.5, 1 and 3 W with an actual applied power of 5, 5 and 6 W, respectively. The substrate was continuously rotated at 60 rpm to ensure composition and thickness uniformity. A constant deposition time of 20 min for all layers yielded film thicknesses of 75-100 nm, as determined by X-ray reflectivity (XRR).

X-ray photoelectron spectroscopy (XPS) spectra were acquired using Al K_α radiation (1486.6 eV) in a PHI 5000 Versaprobe™ system with a hemispherical analyzer and an 8-channel detector. The samples were analyzed after exposure to air but without any sputter cleaning of their surfaces, such that the XPS results are not affected by preferential sputtering which has been reported to lead to, for example, a 12% reduction of the N-to-Ti ratio during sputter cleaning of TiN with 3 keV Ar^+ ions.[45] High-resolution spectra around of the Al 2p, Mg 1s, Ti 2p and N 1s peaks were collected using a 23.5 eV pass energy, a 0.2 eV step size, and a 1.2 eV electron flood gun in conjunction with a low-energy (7 eV) ion neutralizer to compensate for possible surface charging. The composition was determined from the relative peak intensities corresponding to the area under the curves after subtraction of the background

using the Shirley correction, and employing the relative sensitivity factors from the PHI MultiPak software package.

X-ray diffraction was done using a Panalytical X'Pert PRO MPD system with a Cu Kα source and a parallel-beam configuration with an X-ray mirror and a PIXcel solid-state line detector. Sample alignment included height adjustment as well as correction of the ω and χ tilt angles by maximizing the substrate peak intensity. Symmetric ω-2θ scans were obtained using a 0.04 radian Soller slit in front of a PIXcel line detector operated in receiving mode with a 0.165 mm active length, corresponding to a 2θ opening of less than 0.04°. ω-rocking curves were obtained using constant 2θ angles corresponding to $(Ti_{1-x}Mg_x)_{0.25}Al_{0.75}N$ 0002 reflections and using the same parallel beam geometry as used for ω-2θ scans. Asymmetric reciprocal space maps (RSMs) around $10\bar{1}3$ reflections were obtained using a small angle (below 10°) between the sample surface and the diffracted beam to cause beam narrowing which increases the 2θ resolution and therefore facilitates fast high-resolution reciprocal space mapping by taking advantage of parallel acquisition with all 255 channels of a line detector operated in scanning mode. XRD φ scans were obtained using a point focus optics with a poly-capillary x-ray lens that provides a quasi-parallel Cu K_α beam with a divergence of less than 0.3° to minimize defocusing effects associated with the non-uniform sample height due to the tilt of the sample surface normal relative to the plane defined by incoming and diffracted beams. In addition, ω-2θ scans with a divergent beam Bragg-Brentano geometry were acquired over a large 2θ range from 5-85° in order to detect small inclusions of possible secondary phases or misoriented grains.

Optical ultraviolet-to-visible (UV-Vis) transmittance T and reflectance R spectra were collected in a Perkin-Elmer Lambda 950 photospectrometer over the wavelength range 175-3300 nm in 2.5-nm-steps. The reflectance spectra were obtained using a 6° incident angle and were calibrated using an Al mirror reference that was cross-calibrated with the polished surface of a double-side polished MgO(001) substrate and optical constants of MgO from Palik's

handbook.[24c] All optical analyses assume normal incident light for reflection instead of the experimental 6°, which causes a negligible (<1%) error in the presented data. Both collected T and R spectra are treated using a three-media model (air/film/substrate) which assumes the light passing from air to a thin film of constant thickness and parallel surfaces (top and bottom) to a semi-infinite substrate.[46] The experimental measurement error in combination with the approximations in the optical analysis results in an estimated ±5% uncertainty in the reported refractive indices. The absorption within the sapphire substrates is accounted for but results in a negligible correction in comparison to non-absorbing media for the investigated wavelength range. The optical absorption coefficient α is obtained from the measured T and R using $\alpha = \ln([1-R]/T)/d$,[47] where d is the layer thickness. This approximate expression accounts for reflection at the layer surface but neglects multiple reflections within the layer, which are negligible for sufficiently absorbing media. This approach is therefore suitable for determination of the optical gap from α vs. $\hbar\omega$ plots, as confirmed by our measured AlN bandgap of 6.05 eV which is in good agreement with the reported range of 5.90 - 6.25 eV.[1b, 25]

The longitudinal acoustic wave velocity v_{0001} along the growth direction is determined from the picosecond delay in acoustic signals[48] produced in an optical pump-probe technique in a standard two-tint time-domain thermoreflectance (TDTR) set up.[49] For this purpose, the $(Ti_{1-x}Mg_x)_{0.25}Al_{0.75}N(0001)$ layers are coated with an 80-nm-thick Al film that facilitates near-surface optical absorption and serves as an opto-mechanical transducer for a modulated sub-picosecond optical pulse train that periodically heats the sample surface at a frequency of 8.4 MHz. Each incident pulse launches a strain wave at the surface of the aluminum that propagates through the aluminum and either reflects or transmits at the aluminum/film interface based on the mismatch in acoustic impedance between the films. The portion of the strain wave that transmits through the aluminum/film interface proceeds to the film/substrate interface and, again, either reflects or transmits. The reflected strain wave from this interface returns to the

surface of the sample and momentarily alters the optical reflectivity, which is detected by the probe beam. The time-dependent thermoreflectivity signal is used to measure the time difference between the reflected wave from the Al/film and film/substrate interfaces, yielding the sound speed in the film with a known thickness.[50]

Acknowledgements
The authors acknowledge financial support by the National Science Foundation under Grant Nos. 1712752 and 1629230 and the Office of Naval Research MURI Grant No. N0014-18-1-2429.

Received: ((will be filled in by the editorial staff))
Revised: ((will be filled in by the editorial staff))
Published online: ((will be filled in by the editorial staff))

References

[1] a) C. Wood, D. Jena, *Polarization effects in semiconductors: from ab initio theory to device applications*, Springer Science & Business Media, **2007**; b) R. Deng, S. R. Evans, D. Gall, *Appl. Phys. Lett.* **2013**, 102, 112103.

[2] a) Y. Q. Fu, J. K. Luo, N. T. Nguyen, A. J. Walton, A. J. Flewitt, X. T. Zu, Y. Li, G. McHale, A. Matthews, E. Iborra, H. Du, W. I. Milne, *Progress in Materials Science* **2017**, 89, 31; b) B. Liu, X. Chen, H. Cai, M. Mohammad Ali, X. Tian, L. Tao, Y. Yang, T. Ren, *Journal of Semiconductors* **2016**, 37, 021001; c) G. Chen, X. Zhao, X. Wang, H. Jin, S. Li, S. Dong, A. J. Flewitt, W. I. Milne, J. K. Luo, *Scientific Reports* **2015**, 5, 9510; d) L. García-Gancedo, Z. Zhu, E. Iborra, M. Clement, J. Olivares, A. J. Flewitt, W. I. Milne, G. M. Ashley, J. K. Luo, X. B. Zhao, J. R. Lu, *Sensors and Actuators B: Chemical* **2011**, 160, 1386; e) L. V. Minh, H. Kuwano, presented at 2017 IEEE 30th International Conference on Micro Electro Mechanical Systems (MEMS), 22-26 Jan. 2017, **2017**; f) Z. Yang, S. Zhou, J. Zu, D. Inman, *Joule* **2018**, 2, 642.

[3] a) M. Akiyama, T. Kamohara, K. Kano, A. Teshigahara, Y. Takeuchi, N. Kawahara, *Advanced Materials* **2009**, 21, 593; b) G. Wingqvist, F. Tasnádi, A. Zukauskaite, J. Birch, H. Arwin, L. Hultman, *Applied Physics Letters* **2010**, 97, 112902; c) R. Matloub,

A. Artieda, C. Sandu, E. Milyutin, P. Muralt, *Applied Physics Letters* **2011**, 99, 092903; d) M. Moreira, J. Bjurström, I. Katardjev, V. Yantchev, *Vacuum* **2011**, 86, 23.

[4] a) F. Tasnádi, B. Alling, C. Höglund, G. Wingqvist, J. Birch, L. Hultman, I. A. Abrikosov, *Physical Review Letters* **2010**, 104, 137601; b) C. Tholander, I. A. Abrikosov, L. Hultman, F. Tasnádi, *Physical Review B* **2013**, 87, 094107; c) T. Katsunori, K. Junichiro, N. Yoshiro, U. Mamoru, *Japanese Journal of Applied Physics* **2017**, 56, 058004; d) K. Hirata, H. Yamada, M. Uehara, S. A. Anggraini, M. Akiyama, *ACS Omega* **2019**, 4, 15081.

[5] a) C. Tholander, F. Tasnádi, I. A. Abrikosov, L. Hultman, J. Birch, B. Alling, *Phys. Rev. B* **2015**, 92, 174119; b) I. Yoshiki, Y. Tsuyoshi, N. Tokihiro, U. Masanori, *Applied Physics Express* **2015**, 8, 061501.

[6] N. Farrer, L. Bellaiche, *Physical Review B* **2002**, 66, 201203.

[7] S. A. Anggraini, M. Uehara, K. Hirata, H. Yamada, M. Akiyama, *Ceramics International* **2020**, 46, 4015.

[8] a) H. H. Nguyen, L. V. Minh, H. Oguchi, H. Kuwano, presented at 2018 IEEE Micro Electro Mechanical Systems (MEMS), 21-25 Jan. 2018, **2018**; b) H. H. Nguyen, L. V. Minh, H. Oguchi, H. Kuwano, *Journal of Physics: Conference Series* **2018**, 1052, 012018; c) H. H. Nguyen, H. Oguchi, L. Van Minh, H. Kuwano, *ACS Combinatorial Science* **2017**, 19, 365; d) H. H. Nguyen, H. Oguchi, H. Kuwano, *Journal of Physics: Conference Series* **2016**, 773, 012075.

[9] M. Uehara, H. Shigemoto, Y. Fujio, T. Nagase, Y. Aida, K. Umeda, M. Akiyama, *Applied Physics Letters* **2017**, 111, 112901.

[10] a) T. Yokoyama, Y. Iwazaki, Y. Onda, T. Nishihara, Y. Sasajima, M. Ueda, *IEEE Transactions on Ultrasonics, Ferroelectrics, and Frequency Control* **2015**, 62, 1007; b) L. V. Minh, M. Hara, T. Yokoyama, T. Nishihara, M. Ueda, H. Kuwano, *IEEE Transactions on Ultrasonics, Ferroelectrics, and Frequency Control* **2015**, 62, 2005; c)

T. Yokoyama, Y. Iwazaki, Y. Onda, T. Nishihara, Y. Sasajima, M. Ueda, *IEEE Transactions on Ultrasonics, Ferroelectrics, and Frequency Control* **2014**, 61, 1322.

[11] S. A. Anggraini, M. Uehara, H. Yamada, M. Akiyama, *Scripta Materialia* **2019**, 159, 9.

[12] S. Fichtner, N. Wolff, F. Lofink, L. Kienle, B. Wagner, *Journal of Applied Physics* **2019**, 125, 114103.

[13] N. Sinha, G. E. Wabiszewski, R. Mahameed, V. V. Felmetsger, S. M. Tanner, R. W. Carpick, G. Piazza, *Applied Physics Letters* **2009**, 95, 053106.

[14] P. Chakraborty, S. S. Mahato, T. K. Maiti, M. K. Bera, C. Mahata, S. K. Samanta, A. Biswas, C. K. Maiti, *Microelectronic Engineering* **2009**, 86, 299.

[15] a) K.-K. Lee, G. Namkoong, S. M. Madison, S. E. Ralph, W. A. Doolittle, M. Losurdo, G. Bruno, H. K. Cho, *Materials Science and Engineering: B* **2007**, 140, 203; b) O. Ambacher, J. Smart, J. R. Shealy, N. G. Weimann, K. Chu, M. Murphy, W. J. Schaff, L. F. Eastman, R. Dimitrov, L. Wittmer, M. Stutzmann, W. Rieger, J. Hilsenbeck, *Journal of Applied Physics* **1999**, 85, 3222.

[16] J. Ma, J. Hu, Z. Li, C.-W. Nan, *Advanced Materials* **2011**, 23, 1062.

[17] Y. Zhang, W. Jie, P. Chen, W. Liu, J. Hao, *Advanced Materials* **2018**, 30, 1707007.

[18] a) Y. Tal, *Canadian Journal of Chemistry* **1996**, 74, 870; b) C. Kittel, *Inc., New York* **2005**.

[19] a) J. Xu, J. S. Thakur, F. Zhong, H. Ying, G. W. Auner, *Journal of Applied Physics* **2004**, 96, 212; b) K. Kaya, Y. Kanno, H. Takahashi, Y. Shibata, T. Hirai, *Jpn. J. Appl. Phys.* **1996**, 35, 2782; c) S. Hagedorn, A. Knauer, M. Weyers, F. Naumann, H. Gargouri, *Journal of Vacuum Science & Technology A* **2019**, 37, 020914; d) F. Martin, P. Muralt, M.-A. Dubois, A. Pezous, *Journal of Vacuum Science & Technology A* **2004**, 22, 361; e) T. Kumada, M. Ohtsuka, H. Fukuyama, *AIP Advances* **2015**, 5, 017136.

[20] A. G. Bhuiyan, A. Hashimoto, A. Yamamoto, *Journal of Applied Physics* **2003**, 94, 2779.

[21] B. Wang, D. Gall, presented at 2018 IEEE Nanotechnology Symposium (ANTS), 14-15 Nov. 2018, **2018**.

[22] B. Wang, D. Gall, *Thin Solid Films* **2019**, 688, 137165.

[23] a) S. Liu, K. Chang, S. Mráz, X. Chen, M. Hans, D. Music, D. Primetzhofer, J. M. Schneider, *Acta Materialia* **2018**, DOI: 10.1016/j.actamat.2018.12.004; b) R. Cremer, M. Witthaut, A. von Richthofen, D. Neuschütz, *Fresenius' Journal of Analytical Chemistry* **1998**, 361, 642.

[24] a) M. Kazan, S. Pereira, M. R. Correia, P. Masri, *Journal of Applied Physics* **2009**, 106, 023523; b) S. Shokhovets, R. Goldhahn, G. Gobsch, S. Piekh, R. Lantier, A. Rizzi, V. Lebedev, W. Richter, *Journal of Applied Physics* **2003**, 94, 307; c) E. D. Palik, *Handbook of optical constants of solids*, Academic press, **1998**; d) R. Deng, K. Jiang, D. Gall, *J. Appl. Phys.* **2014**, 115, 013506.

[25] a) C. E. Lekka, P. Patsalas, P. Komninou, G. A. Evangelakis, *Journal of Applied Physics* **2011**, 109, 054310; b) N. Pliatsikas, A. Siozios, S. Kassavetis, G. Vourlias, P. Patsalas, *Surf. Coat. Technol.* **2014**, 257, 63; c) D. y. Wang, Y. Nagahata, M. Masuda, Y. Hayashi, *Journal of Vacuum Science & Technology A* **1996**, 14, 3092; d) H. Yamashita, K. Fukui, S. Misawa, S. Yoshida, *Journal of Applied Physics* **1979**, 50, 896.

[26] R. Deng, B. D. Ozsdolay, P. Y. Zheng, S. V. Khare, D. Gall, *Phys. Rev. B* **2015**, 91, 045104.

[27] M. Hiroyoshi, O. Tamio, *Applied Physics Express* **2018**, 11, 041201.

[28] a) J. G. Gualtieri, J. A. Kosinski, A. Ballato, *IEEE Transactions on Ultrasonics, Ferroelectrics, and Frequency Control* **1994**, 41, 53; b) L. E. McNeil, M. Grimsditch, R. H. French, *Journal of the American Ceramic Society* **1993**, 76, 1132.

[29] D. Gall, I. Petrov, P. Desjardins, J. E. Greene, *J. Appl. Phys.* **1999**, 86, 5524.

[30] Q. Long, Y. Li, Y. Wang, *RSC Advances* **2016**, 6, 73063.

[31] a) D. Holec, R. Rachbauer, L. Chen, L. Wang, D. Luef, P. H. Mayrhofer, *Surface and Coatings Technology* **2011**, 206, 1698; b) S. Kassavetis, G. Abadias, G. Vourlias, G. Bantsis, S. Logothetidis, P. Patsalas, *Surf. Coat. Technol.* **2016**, 295, 125; c) G. Greczynski, J. Lu, M. P. Johansson, J. Jensen, I. Petrov, J. E. Greene, L. Hultman, *Surf. Coat. Technol.* **2012**, 206, 4202; d) K. M. Calamba, J. Barrirero, M. P. J. Jõesaar, S. Bruyère, R. Boyd, J. F. Pierson, A. Le Febvrier, F. Mücklich, M. Odén, *Thin Solid Films* **2019**, 688, 137414.

[32] a) L. J. S. Johnson, N. Ghafoor, D. Engberg, M. Thuvander, K. Stiller, M. Odén, L. Hultman, *Thin Solid Films* **2016**, 615, 233; b) N. Ghafoor, L. J. S. Johnson, D. O. Klenov, J. Demeulemeester, P. Desjardins, I. Petrov, L. Hultman, M. Odén, *APL Materials* **2013**, 1, 022105.

[33] Q. Yan, A. Janotti, M. Scheffler, C. G. V. d. Walle, *Applied Physics Letters* **2012**, 100, 142110.

[34] M. Fenker, M. Balzer, H. Kappl, O. Banakh, *Surf. Coat. Technol.* **2005**, 200, 227.

[35] B. Saha, J. A. Perez-Taborda, J.-H. Bahk, Y. R. Koh, A. Shakouri, M. Martin-Gonzalez, T. D. Sands, *Phys. Rev. B* **2018**, 97, 085301.

[36] S. A. Anggraini, M. Uehara, H. Yamada, M. Akiyama, *Materials Letters* **2018**, 219, 247.

[37] a) N. Kurz, A. Ding, D. F. Urban, Y. Lu, L. Kirste, N. M. Feil, A. Žukauskaitė, O. Ambacher, *Journal of Applied Physics* **2019**, 126, 075106; b) M. Baeumler, Y. Lu, N. Kurz, L. Kirste, M. Prescher, T. Christoph, J. Wagner, A. Žukauskaitė, O. Ambacher, *Journal of Applied Physics* **2019**, 126, 045715.

[38] N. B. Sedrine, A. Zukauskaite, J. Birch, L. Hultman, V. Darakchieva, *Japanese Journal of Applied Physics* **2013**, 52, 08JM02.

[39] F. Litimein, B. Bouhafs, Z. Dridi, P. Ruterana, *New Journal of Physics* **2002**, 4, 64.

[40] K. Balasubramanian, S. V. Khare, D. Gall, *Acta Mater.* **2018**, 159, 77.

[41] a) M. Ullah, G. Murtaza, S. M. Ramay, A. Mahmood, *Mater. Res. Bull.* **2017**, 91, 22; b) E. Orhan, S. Jobic, R. Brec, R. Marchand, J. Y. Saillard, *J. Mater. Chem.* **2002**, 12, 2475.

[42] I. H. Nwigboji, J. I. Ejembi, Y. Malozovsky, B. Khamala, L. Franklin, G. Zhao, C. E. Ekuma, D. Bagayoko, *Materials Chemistry and Physics* **2015**, 157, 80.

[43] S. A. Anggraini, M. Uehara, H. Yamada, M. Akiyama, presented at 2017 IEEE SENSORS, 29 Oct.-1 Nov. 2017, **2017**.

[44] E. Milosevic, S. Kerdsongpanya, M. E. McGahay, B. Wang, D. Gall, *IEEE Trans. Electron Devices* **2019**, 66, 3473.

[45] a) R. T. Haasch, T.-Y. Lee, D. Gall, J. E. Greene, I. Petrov, *Surf. Sci. Spectra* **2000**, 7, 204; b) N. Finnegan, R. T. Haasch, D. Gall, S. Kodambaka, J. E. Greene, I. Petrov, *Surf. Sci. Spectra* **2000**, 7, 93.

[46] a) O. S. Heavens, *Optical properties of thin solid films*, Courier Corporation North Chelmsford, MA **1991**; b) B. Wang, S. Kerdsongpanya, M. E. McGahay, E. Milosevic, P. Patsalas, D. Gall, *J. Vac. Sci. Technol. A* **2018**, 36, 061501.

[47] D. Gall, I. Petrov, J. E. Greene, *J. Appl. Phys.* **2001**, 89, 401.

[48] a) C. Thomsen, H. T. Grahn, H. J. Maris, J. Tauc, *Physical Review B* **1986**, 34, 4129; b) C. Thomsen, J. Strait, Z. Vardeny, H. J. Maris, J. Tauc, J. J. Hauser, *Physical Review Letters* **1984**, 53, 989.

[49] K. Kang, Y. K. Koh, C. Chiritescu, X. Zheng, D. G. Cahill, *Review of Scientific Instruments* **2008**, 79, 114901.

[50] G. T. Hohensee, W.-P. Hsieh, M. D. Losego, D. G. Cahill, *Review of Scientific Instruments* **2012**, 83, 114902.